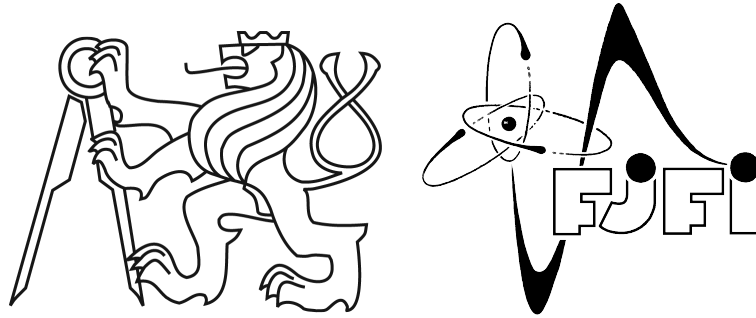


**CZECH TECHNICAL UNIVERSITY IN PRAGUE**  
**Faculty of Nuclear Sciences and Physical Engineering**

**Department of Physics**  
**Branch: Physical Engineering**  
**Specialization: Physics and Technology of Nuclear Fusion**



**Diagnostics Systems for  
Laser-Accelerated  
Particle Beams**

Research project

Author: **Jan Prokúpek**  
Supervisor: **Dr. Daniele Margarone, PhD.**  
Consultant: **RNDr. Josef Krása, CSc.**  
Year: **2010**



## **Acknowledgements**

I would like to express my thanks to Dr. Daniele Margarone for his invaluable support, patience, encouragement, supervision and useful suggestions throughout this work. His moral support and guidance enabled me to complete my work successfully.

Title: **Diagnostics Systems for Laser-Accelerated Particle Beams**  
Author: Jan Prokúpek  
Branch: Physical Engineering  
Work: Research project  
Supervisor: Dr. Daniele Margarone, PhD.  
Institute of Physics of the AS CR  
Consultant: RNDr. Josef Krása, CSc.  
Institute of Physics of the AS CR

**Abstract:**

High energy particles can be accelerated by means of high intensity laser beams - target/plasma interaction via non-linear forces. Recent progress in laser technology enables producing highly collimated quasi-monoenergetic electron beams and high current ion beams. A design of an experimental setup along with precise description of its parts is the first step to achieve best results. Charged particle beams can be deflected by static electric and magnetic fields and further detected by sets of devices which have to be calibrated in proper way. One of the measuring techniques for the ion beam energy is a time of flight method which can also give information about the particle beam intensity. The main stress is given to test the new real-time detectors such as Diamond detector and SiC nuclear detector plus a development of new Farraday cup system. First preliminary test of the detector system was done at PALS laboratory.

Key words: laser, plasma, particle accelerators, electron and ion streams, high energy particle diagnostics.

# Contents

<b>Contents</b>	<b>5</b>
<b>Introduction</b>	<b>6</b>
<b>1 Ion acceleration mechanism</b>	<b>7</b>
1.1 Target normal sheath acceleration . . . . .	7
1.2 Skin-layer ponderomotive acceleration . . . . .	7
1.3 Brief history . . . . .	8
<b>2 Diagnostic systems</b>	<b>10</b>
2.1 Thomson parabola . . . . .	10
2.2 Ion energy analyser . . . . .	12
2.3 Diamond detector . . . . .	14
2.4 SiC nuclear detector . . . . .	15
2.5 Ion Collector . . . . .	18
<b>3 Experimental results</b>	<b>29</b>
<b>Summary and Conclusions</b>	<b>36</b>
<b>Bibliography</b>	<b>37</b>

# Introduction

The concept of particle acceleration by means of laser-plasma interaction is known for more than 30 years. The increasing potential of the laser technologies give as an opportunity to increase the energy of the laser beam and also to decrease the pulse length from a nanosecond-scale to a picoseconds scale. Further progress in laser technologies namely the Chirped Pulse Amplification (CPA) permitted to build laser facilities ranging from a few TW to PW scale powers using pulses of tens of fs.

This increase of laser powers allows us to do a various measurements for understandings a laser-matter interaction, to study plasma behaviour in such conditions and also to observe the plasma and/or particle streams. Once irradiated target produces such possibilities we can use various measurements to observe these condition. The aim of our interest is to observe laser-generated particle streams by means of a time-of-flight (TOF) technique using a real-time diagnostics. Our detection system consists of a diagnostics capable to register particles delivered from laser-irradiated target to the detector.

The diagnostics we tested during our experiment is a Thomson parabola where particles trajectories are bent by applying static electric and magnetic field, electrostatic Ion Energy Analyser where particles with certain energy-to-mass ratio can come through to be detected, Diamond detector and SiC nuclear detector sensitive to the particle energy and Ion collector sensitive to the particle charge state and velocity. Ion collector is developed to register up to four signals at a time and the structure of the detector is further described along with a filtering technique. The filtering technique is useful to cut the radiation coming from plasma letting particles with a sufficient energy to come through and be further detected.

In our experiment will be tested new targets using our diagnostics system. Specially designed and fabricated hydrogen-enriched silicon targets are supposed to deliver higher proton current in comparison with a pure silicon targets.

In our experiments we will use a Prague Asterix Laser System (PALS) which is a high-power iodine laser system capable of delivering up to 1 kJ of energy at the fundamental wavelength 1315  $\mu\text{m}$  at a pulse length about 300 ps. During the experiment the diagnostics will be tested and the results discussed.

This research project is connected to the Bachelor's degree project done the previous year.

# Chapter 1

## Ion acceleration mechanism

Efficient generation of ion beams is observed due to the interaction of high power laser pulses with solid targets. We will describe two different regimes of laser-driven ion acceleration. In both regimes, the laser beam is focused onto a solid target producing a hot ionized plasma. The plasma emits neutral particles, electrons and ions but also UV and X radiation.

### 1.1 Target normal sheath acceleration

The first regime is the target normal sheath acceleration (TNSA) where an ultra-intense short laser pulse is focused onto the front surface of a thin solid target producing plasma and fast electrons [1]. Varying laser intensities from  $10^{17}$  W/cm<sup>2</sup> to  $10^{20}$  W/cm<sup>2</sup> the electrons reach temperatures from 10 keV to 10 MeV. Electrons penetrate through the solid target and at the rear surface they form a Debye sheath effecting as a virtual cathode where the induced electric field is:

$$E_{in} = T/e\lambda_D \quad (1.1)$$

for  $\lambda_{De} = 1$   $\mu\text{m}$  and the mentioned laser intensities of  $10^{17}$  W/cm<sup>2</sup> to  $10^{20}$  W/cm<sup>2</sup> and temperatures of 10 keV to 10 MeV, as mentioned above, the induced field is  $10^{10} - 10^{13}$  V/m. This electric field ionizes atoms at the rear surface of the target and accelerates them. Assuming an acceleration distance ( $L_a$ ) of 10  $\mu\text{m}$ , the ion energy for a certain charge state  $z$  is defined as:

$$\epsilon = zeL_a E_{in} \quad (1.2)$$

and for the mentioned parameters and for the charge state  $z = 1$  the ions can gain energies from 0.1 MeV to 100 MeV. These ions are accelerated mostly in the direction perpendicular to the target layer, for this reason the angular divergence of the beam is mostly less than  $20^\circ$  [1]. The front layer consists of a material with high electron density, and the rear layer consists of a hydrogen-rich material, usually metal-hydrogen. The front layer acts as a source of fast electrons and the rear surface acts as a source of hydrogen ions, which are accelerated in the way described above.

### 1.2 Skin-layer ponderomotive acceleration

The second regime is the skin-layer ponderomotive acceleration (SLPA) where light ions are generated. In this regime mainly plastic thick targets are used. The pre-pulse of the

laser beam ionizes the front side of the target creating a preplasma layer - the skin-layer, which thickness have to be much less than the focal spot diameter of the laser [1]. The laser prepulse intensity has to be significantly lower than the main laser pulse. This condition is much harder attainable for relativistic laser intensities. The main laser pulse interacts intensively with the skin-layer near the surface at the critical electron density and the geometry of the interaction is almost planar. The high plasma density gradient in the interaction region induces two opposite ponderomotive forces which break the plasma and drive two thin plasma blocks towards the vacuum and the plasma interior, respectively [1]. The current density of ions accelerated in the backward direction can be very high. The angular divergence of the ion beam is small due to the almost planar acceleration geometry. In order to reach ion energies in the MeV range, relativistic laser intensities have to be used.

By means of the TNSA method, using relativistic laser intensities and high laser energies, proton beams with currents comparable to the subrelativistic SLPA method can also be produced. In other words, at the same laser intensity, the produced proton current density is much higher for SLPA than for TNSA. Proton density at the source is about thousand times higher in SLPA than in TNSA.

The main problems concerning the generation of heavy ions are related to the ionization efficiency of high charge state ions, and to the acceleration of these ions without any loss of charge state due to recombination effects. The basic principle of atom ionisation is the collisional ionisation caused by inelastic collisions of free electrons which were previously accelerated by the interaction with the laser pulse. If the medium is dense enough, the ionization will be more efficient. This mechanism of producing highly charged ions is more attainable in the case of the short pulses, providing higher laser intensities than for the long pulse ones. However, it is more difficult to obtain highly charged ions far from the expansion zone because of the short interaction time of the short-pulses with the plasma and the consequent rapid adiabatic cooling of the produced plasma with electron-ion recombination.

The SLPA mechanism with double-layer effect in expanding plasma can be used for long laser pulses. The fast electrons come from one layer in front of the expanding plasma and cause the ion acceleration, accelerating first the ions of the highest charge state according to the highest  $z/A$  ratio (the charge state over the mass number of the atom) [1]. When the TNSA mechanism is used the laser intensity has to be greater than  $10^{19}$  W/cm<sup>2</sup> because the electric field produced by the fast electrons has to be high in order to obtain high charge states at the rear surface [1].

### 1.3 Brief history

In Los Alamos National Laboratory was performed an experiment of accelerating Palladium and Carbon ions using neodymium-glass laser (based on CPA) and TNSA double-layer acceleration method [2]. Heating the target to temperatures higher than 1100 K, complete dehydrogenization was performed and carbon compounds formed very thin graphite layer at the monolayer scale on the surface of the palladium foil of thickness 20  $\mu\text{m}$ . The graphite layer was used as the rear side of the target. Acceleration of  $\text{C}^{5+}$  and  $\text{C}^{6+}$  ions and also  $\text{Pd}^{22+}$  ions (which are the next highest charge-to-mass ratio ions) was observed. According to the highest charge-to-mass ratio the  $\text{C}^{5+}$  ions were dominantly accelerated and had a monoenergetic distribution with a mean energy of 36 MeV, whereas Pd ions had a typical exponential spectrum.

At the University of Jena an experiment using JETI Ti:Sapph laser (based on CPA) and TNSA double-layer acceleration method was performed [3]. The solid target was a

5  $\mu\text{m}$  thin titanium foil (thinner foil would result in higher proton energies but according to reproducibility of the experiment the thicker target was chosen). On the rear side of the foil there were dots made of polymethylmethacrylate (PMMA). This hydrogen-rich PMMA dots were constructed by the femtosecond laser ablation and they were made only for one single shot. The laser pulse hitting the target exactly on the opposite side of the PMMA dots, generated a peak of proton energy at 1.2 MeV. It is expected, that gold target could deliver more hot electrons to be used for accelerating protons.

## Chapter 2

# Diagnostic systems

### 2.1 Thomson parabola

The Thomson parabola (TP) is a mass spectrograph. Charged particles propagate through the TP and are deflected by static electric and magnetic fields parallel to each other and perpendicular to the motion of the charge particle stream. The stream is registered at the imaging plane.

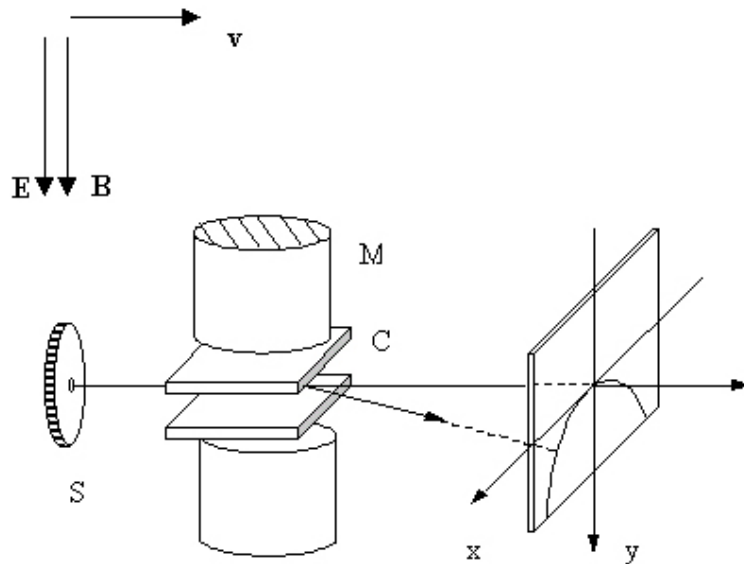


Figure 2.1: Thomson parabola analyzer. Particle stream propagates through the parallel  $\mathbf{E}$  and  $\mathbf{B}$  field initiated by permanent magnet  $M$  (or electromagnet) and capacitor  $C$  and ions are separated due to their charge-to-mass ratio and impact the imaging plane.

Ions are influenced by the electric and magnetic field and their trajectory is a consequence of the laws of motion, i.e. when charged particles enter the direction perpendicular to the parallel fields, the particles will draw the parabola on the imaging plane. The equation of the drawn parabola is

$$y^2 = \frac{z}{M} \frac{eB^2LD}{E} x \quad (2.1)$$

where  $B$  and  $E$  are magnetic and electric parallel fields,  $L$  is the length of the capacitor and  $D$  is distance from the end of the capacitor to the registration plane. For  $C^{5+}$  ion,

capacitor length  $L = 10$  cm, distance from capacitor to imaging plane  $D = 20$  cm, magnetic field  $B = 1$  mT, voltage on capacitor  $V = 1$  kV, distance between capacitor plates  $b = 2$  cm, thus electric field is  $20 \text{ Vm}^{-1}$ , coordinate  $x = 5$  cm the  $y$  coordinate according to equation 2.1 is 4.48 cm.

The ion energy  $\epsilon$  can be determined e.g. from the  $x$  coordinates which is equal to

$$x = DL \frac{zeE}{2\epsilon} \quad (2.2)$$

The energy from equation 2.2, taking into account the above reported values, is  $\epsilon = 20$  eV.

Both  $x$  and  $y$  coordinates depend on the ion energy. The point of origin of the plane is given by the impact of neutral particles and X-UV radiation from plasma. It is seen from equation 2.1 that an ion stream with a certain value of the charge-to-mass ratio will draw a different parabola than for streams with different ratios. From equation 2.2 it is seen that more energetic particles are closer to the apex of the parabola. Recording system of TP can have two different types of detectors, track detectors or image converter with an MCP of high diameter as an amplifier [4]. The widths of the parabolas are influenced by the quantity and charge state of the ions, the time of flight and the geometry of the measurements. It can also be seen from the experiments that ions of certain charge-to-mass ratio with lower energy are more affected by the space charge than ions with higher energy, thus the parabola is wider for ions with lower energy.

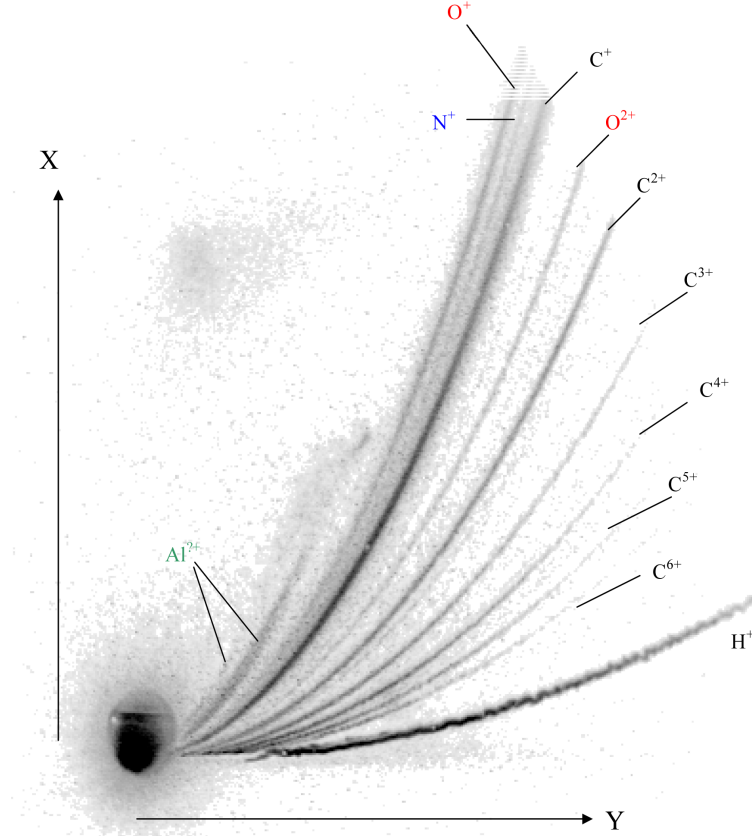


Figure 2.2: Typical TP spectrum. The graphite target was used with the oxygen, hydrogen and nitrogen impurities.

## 2.2 Ion energy analyser

The ion energy analyser (IEA) is a device aimed to determine ion energy distributions and abundances of ion species in the plasma [4]. The main part of the IEA is a deflection system consisting of two coaxial metallic cylinders ( $R_1$  inner radius and  $R_2$  outer radius) charged at a proper potential ( $V_1$  and  $V_2$ ). The schematic draw of the IEA is reported in figure 2.3.

The ion trajectory is deflected by a radial electric field inside the deflection system. When the equilibrium between the centripetal force acting on an ion with charge state  $z$  and the force affecting the ion in the radial electric field of the deflection system occurs, the energy-to-charge state ratio is:

$$\frac{E}{z} = \frac{e(V_2 - V_1)}{2 \ln(R_2/R_1)} \quad (2.3)$$

where  $e$  is the elementary charge, the inner radius is  $R_1 = 10.25$  cm and the outer radius is  $R_2 = 10.5$  cm. If the cylinders are charged at potential  $V_2 = -V_1 = 3$  kV and we want to measure the carbon ion  $C^{5+}$ , its energy is  $E = 622$  keV. Considering:

$$E = \frac{1}{2} M v^2 \quad (2.4)$$

where  $M$  is the mass of the ion and  $v$  is the velocity given by the ratio between the

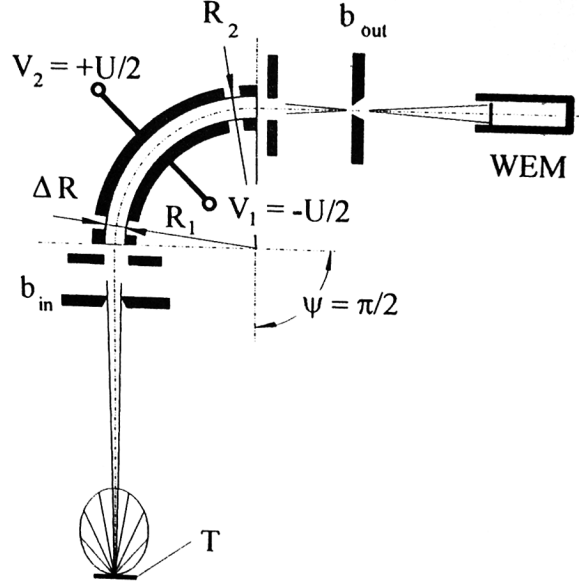


Figure 2.3: Scheme of the IEA. Plasma is produced at the target T heading to the deflection system of the IEA and further to the detector WEM (windowless electron multiplier). The input and output slits  $b_{in}$  and  $b_{out}$  collimate the ion beam entering and leaving the IEA [4].

distance  $L$  of the detector and the time of flight (TOF), i.e. the time needed for ion to reach the distance  $L$ . From equations 2.3 and 2.4 the TOF is

$$\tau = L \sqrt{\frac{M \ln(R_2/R_1)}{z e (V_2 - V_1)}} \quad (2.5)$$

For the same values of  $R_1$ ,  $R_2$ ,  $V_2$  and the distance  $L = 2$  m the time of flight of the  $C^{5+}$  will be  $\tau = 6.3 \times 10^{-7}$  s. As can be seen from equation 2.5 that only ions with certain charge-to-mass ratio can pass through the IEA and reach the detector. The detector WEM registers the voltage caused by the impact of the ions depending on their time of flight. For known IEA parameters and TOF the charge-to-mass ratio is determined from equation 2.5.

The main disadvantage of the IEA is the requirement of a large number of laser shots in order to obtain the ion energy distribution [4]. Moreover, the maximum voltage which is possible to bring on the coaxial metallic cylinders gives the limitation to detection in the maximum proton energy at a value of 0.6 MeV.

## 2.3 Diamond detector



Figure 2.4: Diamond detector.

High purity synthetic Chemical Vapor Deposition (CVD) Diamond presents unique characteristics [5] that make it an excellent material for radiation detection. Depending on the extension of their depletion layer, diamond can detect any kind of radiation that is more energetic than its bandgap of 5.45 eV, e.g., deep UV photons, X-rays, gamma rays, charged particles and neutrons with a dynamic range in energies spanning from 5.5 eV up to GeV of cosmic rays (the convenient for experimental usage is its non-sensitivity to the visible radiation). Because of its radiation hardness it needs no frequent replacements, its high mobility of free charges equates into a very fast response (about 100 ps). Diamond can be operated at room temperature with no need for cooling, it has a resistivity several orders of magnitude greater than silicon, and extremely low leakage current and no need for p-type or n-type junctions as required in the fabrication of silicon radiation detectors [6]. These special characteristics of diamond also allow its use in extreme environmental conditions like high temperature, high radiation, and highly corrosive environments. Hence, its use for example in high energy physics as Beam Condition Monitor and particle tracker at CERN, as a radiotherapy dosimeter, in X-ray synchrotron radiation monitoring (e.g., ESRF in Grenoble) or as UV and neutron detector at the Joint European Torus in Culham [6].

Diamond radiation detectors are generally designed as a parallelepiped solid-state ionization chamber in two main configurations: with electrodes attached at front and back, so called planar (sandwich) configuration, or interdigitated electrodes on the same surface. In the case of sandwich structure the "soft" radiation is absorbed in the metal contact, thus this configuration can be considered suitable when "hard" radiation has to be detected. A charged particle, or a photon with energy above the bandgap, passes through the diamond and ionizes it generating electron-hole pairs (e-h pairs). The energy needed to form e-h pair is 13 eV [6]. Electrons are separated from holes by the electric field between the electrodes. Created charge is then collected by the electrodes and contributes to a photoconductive current in the detector and the current comes also to an external circuit. First radiation detectors from natural diamonds date back to 1945, although earlier experiments were performed in 1920 [7]. At that time (1945), counting properties were found to be uncontrollable, depending upon the crystal and the type of radiation. Furthermore, charge polarization occurred, leading to progressive reduction in both counting rate and pulse amplitude as a function of the time of irradiation [8, 9].

In the past, the polarization phenomenon was due mainly to the high level of impurities present in natural and early CVD diamond. At present the polarization phenomenon can be ascribed to the nature of the metal-diamond interface and not to the bulk of a high

Crystal structure	Diamond
Band structure	Indirect
Energy gap $E_g$	5.45 eV
Electron mobility $\mu_n$	1800 – 22000 cm <sup>2</sup> /Vs
Hole mobility $\mu_p$	1200 – 1600 cm <sup>2</sup> /Vs
Breakdown electric field $E_c$	10 MV/cm
Thermal conductivity $\tau_{th}$	20 W/cm°C
Saturation velocity $v_s$	2.2 – 2.7 × 10 <sup>7</sup> cm/s
Relative dielectric constant $\epsilon_r$	5.5
Maximal working temperature	1100 °C
Evaporation temperature	3500 °C
Electron-hole pair energy	13 eV
Hole lifetime $\tau_p$	10 <sup>-9</sup> s
Density $\rho$	3.52 g/cm <sup>3</sup>
Atomic weight	12
Lattice constant	3.567 Å
Electron affinity	-1.07 V

Table 2.1: Principal properties at room temperature of the Diamond detector employed for diagnostic in laser-generated plasmas.

purity single crystal CVD diamond.

In order to overcome the polarization problems mentioned above and to provide a method for forming an ohmic electrode that makes a good ohmic contact on diamond that is also durable and stable for applications in diamond radiation detectors and diamond electronics thus a novel electrical contact using a very thin diamond like carbon layer was developed and tested [6]. Diamond-like carbon is a form of amorphous carbon between diamond and graphite as can be seen in following figure, containing significant portion of sp<sup>3</sup> bonded atoms in the matrix.

In order to obtain information about the energetic distributions of photons and particles ejected from plasma explosion, diamond detectors can be used in TOF configuration with or without thin foils absorbers or magnetic filters. In fact one of the disadvantages of those detectors is the polarity of the output signal which will be unique, thus it might be difficult to distinguish among different plasma contributions.

Ion current  $I_{DD}$  registered at the output of the diamond detector can be estimated from the formula (2.6), which is valid also for a semiconductor detector:

$$I_{DD} = \frac{en_j m_j u_{eff} U}{2\epsilon d} v_j^2 \quad (2.6)$$

where  $e$  is an elementary charge,  $n_j$ ,  $m_j$  and  $v_j$  are the density, mass and velocity of  $j^{th}$  particle species,  $u_{eff}$  is the semiconductor electron mobility,  $U$  is the applied voltage on the detector,  $\epsilon$  is the permittivity of the diamond and  $d$  is its thickness. Preliminary measurements with diamond detector have been performed at PALS and the result (see plot in figure 2.15) is discussed in chapter 3.

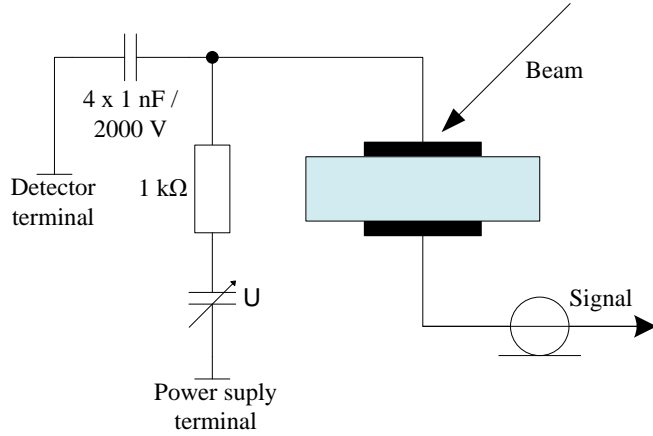


Figure 2.5: Circuit scheme of the Diamond detector.

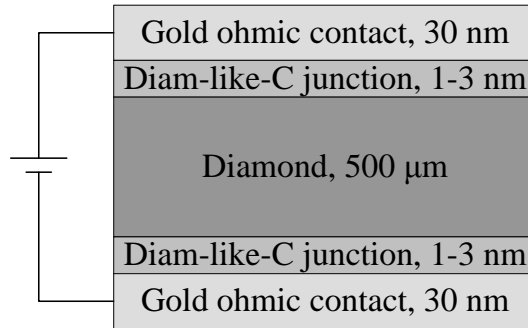


Figure 2.6: Cross-section scheme of the Diamond detector.

## 2.4 SiC nuclear detector

Semiconductor detectors have been used in the last years to monitor the ionizing radiation emitted from laser-generated plasmas and the detectors permitted simultaneous measurements of x-rays emitted during the short life of the pulsed plasma (typically picoseconds-nanosecond scale) and of fast electrons and slower ion emission [10]. SiC detectors producing signals proportional to the energy deposited in its depletion layer by the incident photons and particles, are very attractive because these detectors are not sensitive to the visible and infrared light - optical photons are not capable to produce electron-hole (e-h) pairs because their energy is below the 3.26 eV for 4H-SiC gap energy. Thus these detectors can operate under visible light exposition at which it is transparent.

The main advantages of 4H-SiC-based detectors are radiation hardness, application at high temperature operation with low dark current, high signal-to-noise ratio, high detection efficiency, high energy gap, and controllable depletion layer thickness [11]. Photons, electrons and ions absorbed in the sensitive volume of the detector generate e-h pairs losing 7.78 eV for a pair production, with results in arising voltage signal at the device electrodes that is proportional to the deposited radiation energy. The lack of sensitivity to the visible light permits the use of the SiC detector without any shielding filters to detect simultaneously UV, x-rays, electrons and ion beams from laser-generated plasma. The following table reports the main properties of a SiC detector.

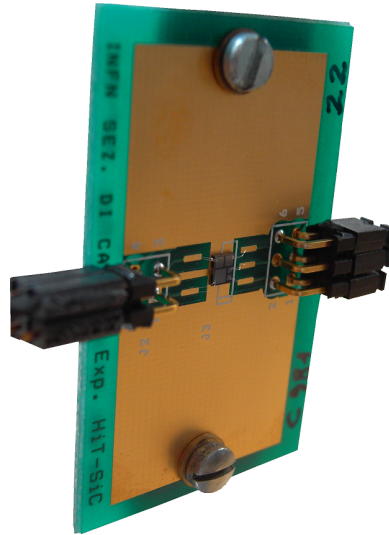


Figure 2.7: SiC detector.

Nitrogen was used as *n*-type doped material at concentration of  $2 \times 10^{14} \text{ cm}^{-3}$ . Metal-semiconductor Schottky diodes were employed depositing  $\text{Ni}_2\text{Si}$  on the Si-*n* doped, generating a rectifying junction (the height of Schottky barrier is 1.7 eV). The thickness of the  $\text{Ni}_2\text{Si}$  metallization is 200 nm.  $\text{Ni}_2\text{Si}$  top layer and Si-*n*+ high doped bottom substrate were contacted with an ohmic Al bonding and were covered by a thin gold deposition layer [10].

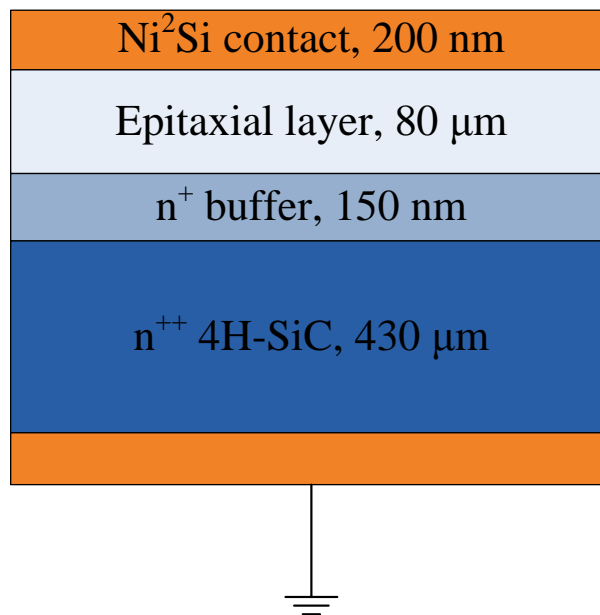


Figure 2.8: Cross-section scheme of the SiC detector.

The SiC diode is usually employed with an electric circuit reported in following figure 2.9. In this configuration at -600 V bias it has energy resolution 34 keV FWHM at 5.8 MeV and 100% charge collection efficiency [10], as demonstrated during detecting alpha particles emitted from a  $^{239}\text{Pu}$ - $^{241}\text{Am}$ - $^{244}\text{Cm}$  source [11, 12].

Crystal structure	Hexagonal
Band structure	Indirect
Energy gap $E_g$	3.26 eV
Electron mobility $\mu_n$	800 – 1000 cm <sup>2</sup> /Vs
Hole mobility $\mu_p$	100 – 115 cm <sup>2</sup> /Vs
Breakdown electric field $E_c$	2.2 – 4.0 MV/cm
Thermal conductivity $\tau_{th}$	3.0 – 5.0 W/cm°C
Saturation velocity $v_s$	0.8 – 2.2 × 10 <sup>7</sup> cm/s
Relative dielectric constant $\epsilon_r$	9.7
Maximal working temperature	1240 °C
Evaporation temperature	1800 °C
Electron-hole pair energy	7.78 eV
Hole lifetime $\tau_p$	6 × 10 <sup>-7</sup> s
Density $\rho$	3.21 g/cm <sup>3</sup>
Atomic weight	44
Lattice constant	$a = 3.07 \text{ \AA}, c = 10.05 \text{ \AA}$
Electron affinity	3.08 V

Table 2.2: Principal properties at room temperature of the 4H-SiC detector employed as diagnostics in laser-generated plasmas [12].

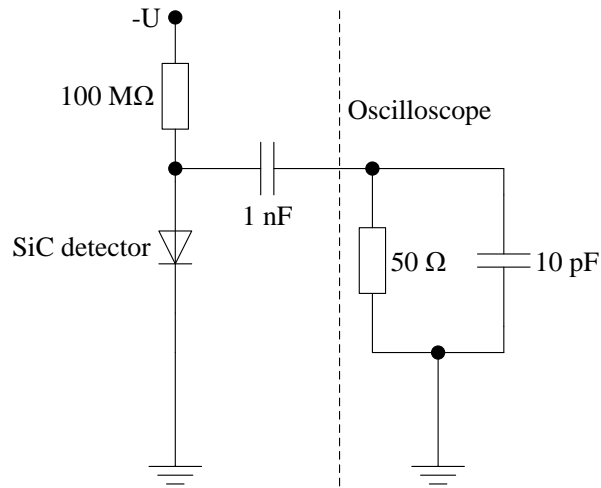


Figure 2.9: Circuit scheme of the SiC detector.

Ion current registered at the output of the SiC nuclear detector can be also estimated from the formula 2.6 mentioned in section 2.3 and the result of the preliminary measurements have been performed at PALS (see plot in figure 2.15) and it is discussed in chapter 3.

## 2.5 Ion Collector

The Ion Collector (IC) is a simple detector (Faraday cup) used for detecting an electrical charge of a laser-plasma produced particle streams. The IC simple detecting system is based on keeping high negative voltage on the detection plate where electrons are repulsed onto the grounded grid in front of the plate and positively charged particles and electromagnetic emission from the plasma can be recorded on the output of the detector by a fast storage oscilloscope. Actually the plasma photopeak radiation is pointed out by means of the secondary electron emission from the collector surface (copper photocathode). The overlapping between the photopeak and high energy plasma ions (mainly fast protons) represents a problem in determination of the maximum ion energy. Thus, in order to cut off the relatively long photopeak and to detect only the positively charged particles a filtering technique can be used by varying types and thicknesses of thin metal foils placed in front of the collector. The ion collector set in our experiment present two main geometries, quadrant or ring configuration, as it can be seen on figure 2.10.

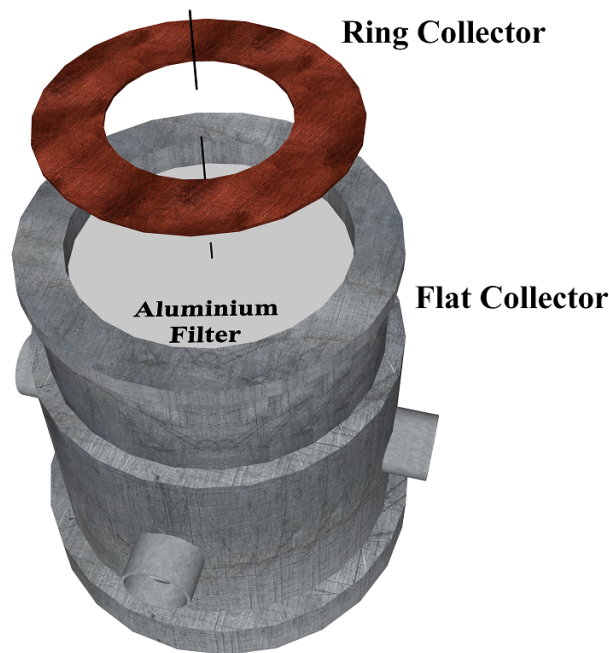


Figure 2.10: Sketch of the flat and ring configuration of the ion collector.

With modified IC one can register up to 4 signals from one detector where different kinds and/or thicknesses of filters can be applied and the outputs can be evaluated as 4 separated signals from 4 different collectors.

The IC in flat configuration exhibits great measuring possibilities itself. The filters can be easily changed by simple demounting this device from the experimental chamber. The only disadvantage of this type of device is the impossibility of adding any other measurement behind this detector to get simultaneous measurements along the same axis from the target. The possible solution of this can be the use of a multi-shielded IC ring configuration. The ring collector is supposed to be set inside a pipe attached to the experimental chamber making the system adaptable to make measurements at different angles from the target normal. The pipe within the collector is grounded separately from the experimental chamber and it also serves as the grounding for the grid of the collector.

The ring IC also permits the possibility to perform various measurement of the plasma

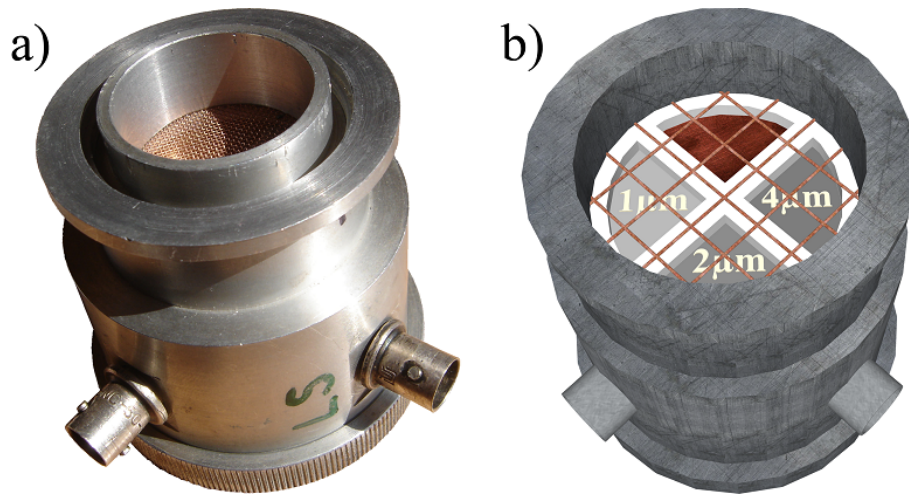


Figure 2.11: a) photo of the flat ion collector used during the experiments, and b) scheme of the four channel flat ion collector with different filtering.

stream on the same axis. Along our experiments we have mostly used diagnostics behind the ring IC such as quadrant IC, Thomson parabola, Ion electrostatic analyzer, diamond and SiC detectors.

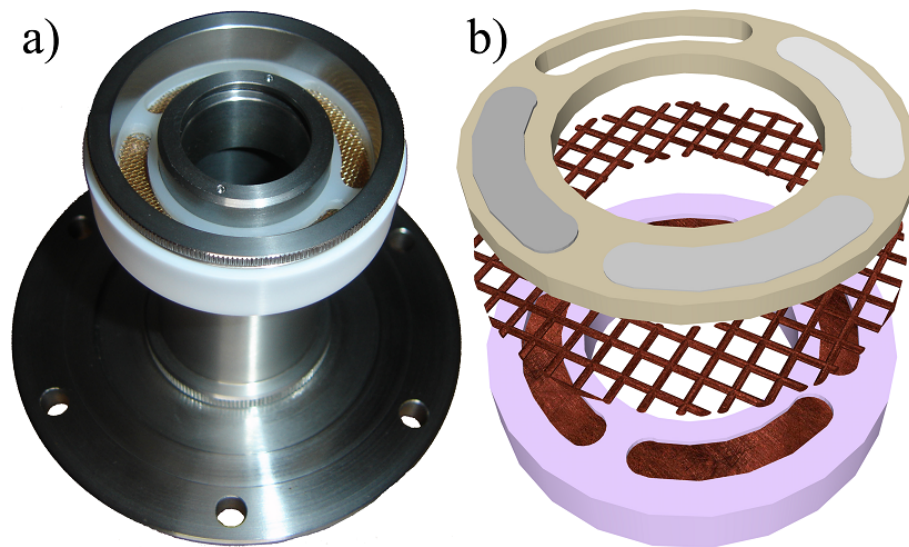


Figure 2.12: a) photo of the ring ion collector separated into the four quadrants, and b) scheme of each part serving as an independent collector which can be shielded by different type of filters.

Ring collector was developed for an upcoming experimental campaign held in January 2010. The ring itself was divided into four pieces and an independent electronic was made for each piece. The electronic part for one piece consists of two resistors, one capacitor, one diode and the groundings. The whole set of four collectors has a common input voltage through the coaxial cable and common one capacitor with grounding. The scheme of the collector can be seen on figure 2.13.

During the experiment the input on the coaxial cable, using impedance of  $50 \Omega$ , is set

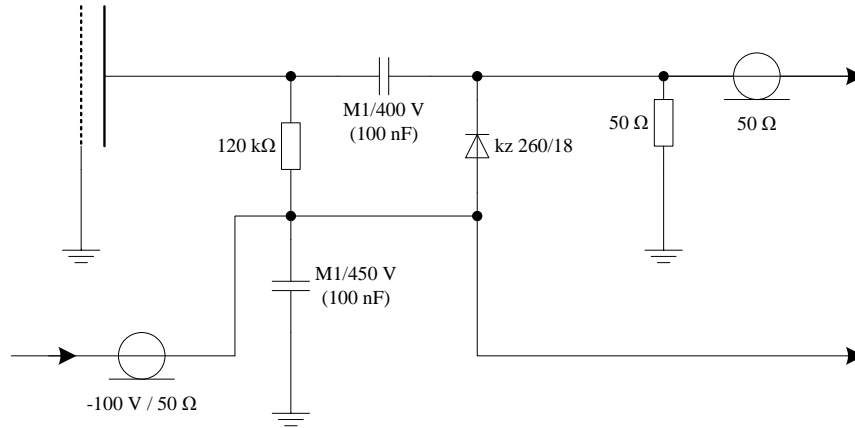


Figure 2.13: Scheme of the circuit of the IC along with the input common for all parts.

on -100 V. The negative voltage is applied to collector plates due to the repulsive force affecting incoming electrons repulsing them onto the grounded grid at the entrance of the collector. A 100 nF capacitor labelled as M1/450 V is common for all collectors inside the device and it serves as a filter on the voltage input. It is used to neglect the influence of all four collectors and also to minimize the interference from the electrical power network or from the coaxial cable itself. The higher capacity on this capacitor, the better should be the minimizing properties, the only problem of this is the output signal on the oscilloscope and thus a compromise should be done for minimizing the interference. On the left bottom of the scheme in figure 2.13 the arrow labels the input for the other electric circuit of the next collector.

The input voltage of each collector plate is coming through the 120 kΩ resistor. This resistor is keeping the voltage on the collector plate and in case of a puncture between the grid and the collector it extinguishes the discharge. If this resistance is too small, the current would go back to the input. Collector plate serves as a current source in the moment of impact of the particles. The current from the recorded signal on the collector plate is coming through the 100 nF capacitor labelled as M1/400 V. This capacitor is placed here for keeping the direct current on the collector plate and does not enable it to pass through; therefore it is not registered by the oscilloscope. The capacitor impedance remains high when the whole system is stationary. Then only the current pulse can come through the capacitor and cause the signal recorded on the oscilloscope.

Parallel to the 120 kΩ resistor is a kz 260/18 diode. The diode is here for the reason of protection the oscilloscope from the pulse overshoot due to the photopulse. It will cut the photopulse and it can also cut the negative signal. If the diode is released from the circuit the photopulse could be as much as 1 μs long. This signal is caused by the photopulse which impacts the collector plate and strike electrons which are collected on the grid. This diode can release the voltage signal up to 18 volts and it is fast enough and convenient for the nanosecond-scale processes. Slower diodes have their own inductance and the influence for the final signal should be properly measured. Also the usage of this diode for sub-nanosecond processes should be tested for its properties on such scales.

The last component, before the signal leaves into the coaxial cable and on the input of the oscilloscope, is a 50 Ω resistor with its grounding. The resistor is placed here because of the output into the 50 Ω coaxial cable. It helps to prevent from the reflections and it reduces the current output signal to one half, the voltage remains the same. We measure on the output signal where real current can be calculated from the measured voltage but

with a resistance of 25  $\Omega$ . If this resistor is released from the circuit the pulse of the same length is added in each measurement caused by the reflection at the end of the cable and this pulse is dependent upon the length of the cables.

There is a question about what we are detecting at the beginning of the pulse. For this purpose there are relevant issues such as changing or calibrating the diode for sub-nanosecond processes and varying the length of the copper cables between the collector plate and the first component of the electric circuit of the IC device. The shortest length of the cables and placing the circuit as close to the collector plate as possible can give as an information about the fast electrons coming right behind the photopeak beginning. Such measurement can give us information about the evolution of the plasma at the target and/or the plasma stream.

As was mentioned above the ion current is collected by a biased collector and it is measured by means of a fast storage oscilloscope. If ions reach the collector it causes the secondary electron-ion emission that may be suppressed by using a metal grid. Neglecting the secondary ion-electron emission and shielding grid the current density is:

$$I_i = en_e v = ev \sum_{j=0}^{Z_{max}} z_j n_{i,j} \quad (2.7)$$

where  $e$  is elementary charge,  $n_e$  is an electron density and  $v$  is the plasma velocity,  $j$  is the number of ion species,  $n_{i,j}$  is the density of the  $j^{th}$  ion specie and  $z_j$  is the charge state of the  $j^{th}$  ion specie. Using the biased collector, the space charge layer is formed and shields the collector from the plasma. The threshold ion density for this effect is approximately given by

$$n_{i,z} [\text{cm}^{-3}] \leq 2.5 \times 10^8 \frac{E [\text{keV}]}{z \cdot d_2 [\text{cm}]} \quad (2.8)$$

where  $E$  is the kinetic energy of ions with the charge state  $z$ ,  $d_2$  is the distance between grid and collector,  $n_{i,z}$  is the density of ions with the charge state  $z$ . It can be seen from equation 2.8 that ions with the lower energy and charge state are more severely limited by the space charge. For a grid-collector distance of 2 cm, ion energy 1 keV for the charge state 5+, the threshold limitation for the ion density is  $2.5 \times 10^6 \text{ cm}^{-3}$ .

The output current  $I_c$  in the collector circuit is a combination of ion current  $I_i$  and secondary electron current  $I_e$ :

$$I_c = I_i + I_e = eevS \left\{ \sum_{j=0}^{Z_{max}} [z_j(t) + \gamma_j(t)] n_{i,j}(t) \right\} \quad (2.9)$$

where  $\epsilon$  is the transparency of the entrance grid,  $S$  is the area of the collector,  $\gamma_j$  is the secondary ion-electron emission coefficient,  $z_j$  is the charge state,  $n_{i,j}$  is the density of the  $j^{th}$  ion species where  $j = 0$  corresponds to the neutral particles. Taking into account that  $n_i = \sum n_{i,j}$  in equation 2.9 we can write

$$I_c(t) = eevS \bar{z}(t) n_i(t) \left[ 1 + \frac{\bar{\gamma}(t)}{\bar{z}(t)} \right] = \epsilon \left[ 1 + \frac{\bar{\gamma}(t)}{\bar{z}(t)} \right] I_{coll}(t) \quad (2.10)$$

where  $\bar{\gamma} = \sum_j \gamma_j n_{i,j} / \sum_j n_{i,j}$  is the average secondary ion-electron emission coefficient,  $\bar{z} = \sum_j z_j n_{i,j} / \sum_j n_{i,j}$  is the average charge state of ions and  $I_{coll}$  is the ion current in

the entrance grid for a given moment  $t$ . Then from equation 2.10 the ion current on the entrance grid is:

$$I_{coll}(t) = \frac{U_C(t)}{\epsilon R_{load} \left[ 1 + \frac{\bar{\gamma}(t)}{\bar{z}(t)} \right]} \quad (2.11)$$

where  $U_C(t)$  is the voltage amplitude of the collector signal and  $R_{load}$  is the load resistance. From equation 2.11 it is also possible to obtain the velocity and energy distribution.

When the laser hits the target, plasma and accelerated ions are generated together with XUV radiation from the plasma. The radiation spreads through the chamber and reaches the IC as first causing a secondary electron emission from the grid and, as a consequence, a voltage amplitude (called photo-peak) at the output signal. The photo-peak serves as a trigger for the time measurements.

This technique permits to have simultaneously information from the whole plasma emission (XUV, fast and slow ions) and only from different ion energy ranges (depending on the filter thickness). The XUV radiation can be cut by using Au and Ta filters of thickness 1–5  $\mu\text{m}$ . The figures below report the transmission of the XUV radiation in different metallic filters [13].

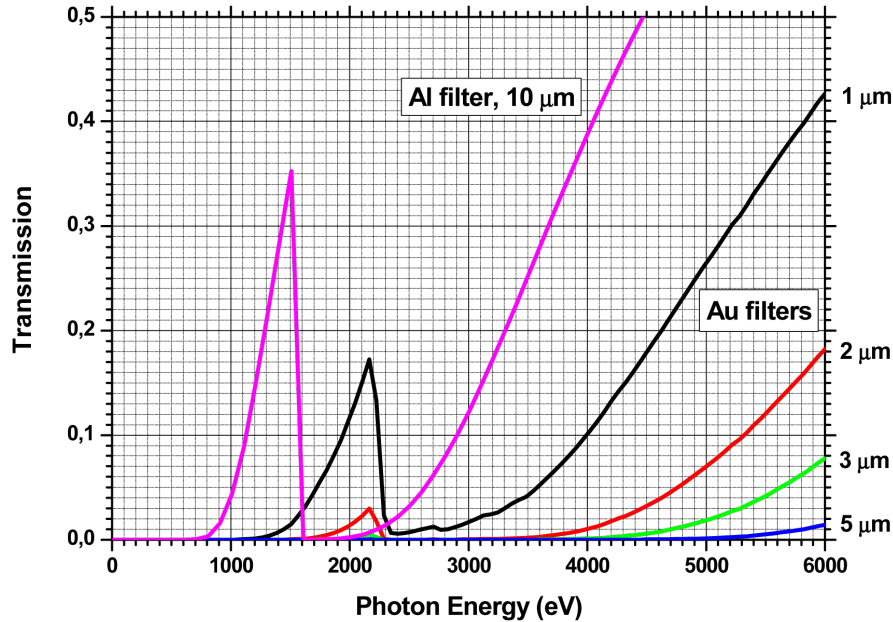


Figure 2.14: Transmission of XUV radiation depending on photon energy for Au filter of thickness 1, 2, 3 and 5  $\mu\text{m}$  and Al filter of thickness 10  $\mu\text{m}$ . The 10  $\mu\text{m}$  Al filter cuts the photon energy less than 800 eV and the 1  $\mu\text{m}$  Au filter cuts the photon energy less than 1.3 keV.

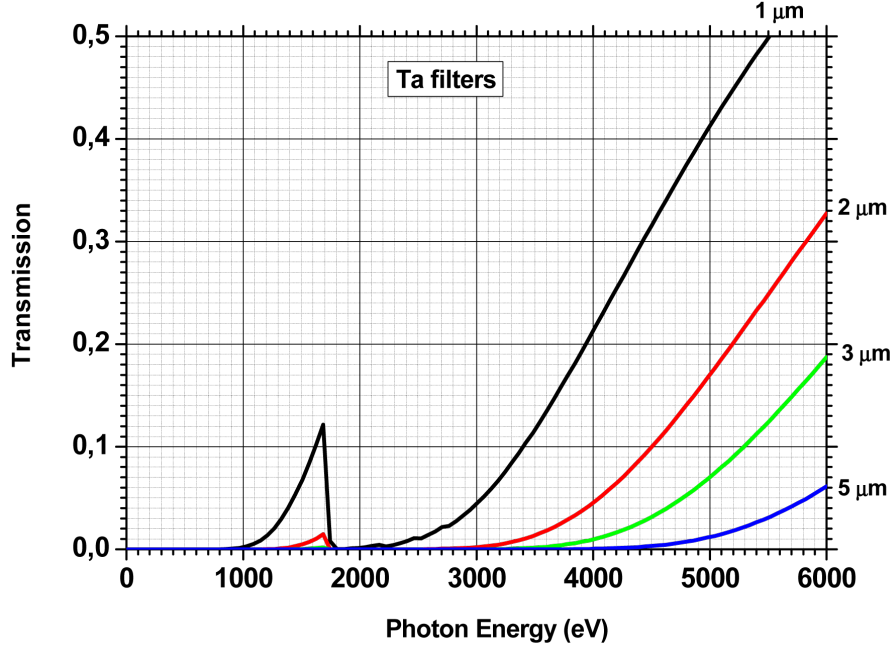


Figure 2.15: Transmission of XUV radiation depending on photon energy for Ta filter of thickness 1, 2, 3 and 5  $\mu\text{m}$ . The 1  $\mu\text{m}$  Ta filter cuts the photon energy less than 1 keV.

The filtering technique causes the spread in energy distributions of the ions due to the interactions with the filter atoms. The energy loss of the ions depends on their own energy. This problem can be reduced if a light element filter is used (e.g. Al filter), but on the other hand, the XUV transmission increases (as reported on figure 2.14). If the filter is placed few millimetres from the IC the change in TOF is negligible because the target-collector distance is usually long, thus the energy spread is negligible. The filter does not cut only the XUV radiation, it also cuts low energy ions and disable their further detection. The cut-off energy can be predicted by SRIM simulations. The table below reports the cut-off energies of the elements in the filter.

SRIM is a group of programs which calculate the stopping and range of ions (10 eV – 2 GeV /amu) into matter using a quantum mechanical treatment of ion-atom collisions. During collisions, the ion and atom have a screened Coulomb collision, including exchange and correlation interactions between the overlapping electron shells. The ion also has long range interactions with target atoms creating electron excitations and plasmons (plasmon is a quantum of a collective oscillation of charges on the surface of a solid induced by a time-varying electric field) within the target. These are described by including a description of the target collective electronic structure and interatomic bond structure when the calculation is setup. The charge-state of the ion within the target is described using the concept of effective charge, which includes a velocity dependent charge state and long range screening due to the collective electron sea of the target [14].

If the ion is not stopped in the filter, it is slowed and its energy decreases, whereas its energy spread increases. The ion energy spread is given as:

$$\sigma = \frac{E_M - E_m}{E_p} \quad (2.12)$$

and it is mainly given at FWHM which means the  $E_p$  is a peak of energy and  $E_M - E_m$  is an energy range at half of the peak.

Ion Beam	Filter Thickness ( $\mu\text{m}$ )	Cut-off Energy of Au filter (MeV)	Cut-off Energy of Ta filter (MeV)	Cut-off Energy of Al filter (MeV)
H	1	0.275	0.25	0.12
H	2	0.5	0.45	0.25
H	3	0.65	0.6	0.325
H	5	1	0.9	0.5
C	1	2	1.7	0.65
C	2	5.5	4.5	1.8
C	3	9	8	3.25
C	5	15	14	6
Ti	1	4.5	4	1.4
Ti	2	13	11	3.5
Ti	3	25	22.5	6.5
Ti	5	60	50	15

Table 2.3: The cut-off energy of H, C and Ti elements in Au, Ta and Al filters in the thickness range 1–5  $\mu\text{m}$  predicted by SRIM simulations.

When the ion has an initial energy  $E_i$  and passes through the filter losing an energy  $\delta E$ , its final energy will be:

$$E_f = E_i - \delta E \quad (2.13)$$

The energy lost caused by the ionization in the filter can be calculated using TRIM simulations.

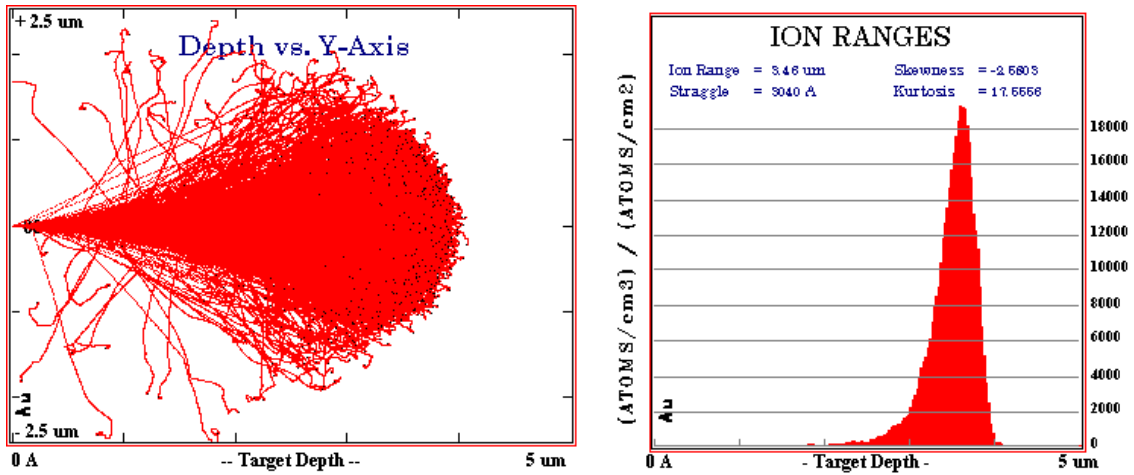


Figure 2.16: Example of longitudinal distribution and the ion ranges inside the Au target by using TRIM simulation for C element with energy of 10 MeV.

TRIM (the Transport of Ions in Matter) is a Monte-Carlo calculation which follows the ion into the target, making detailed calculations of the energy transferred to every target atom collision. TRIM will accept complex targets made of compound materials with up to eight layers, each of different materials. It will calculate both the final 3D distribution of the ions and also all kinetic phenomena associated with the ion's energy loss: target damage, sputtering, ionization, and phonon production. All atom cascades in the target

are followed in detail. The program is made so it can be interrupted at any time, and then resumed later. The calculation is made very efficient by the use of statistical algorithms which allow the ion to make jumps between calculated collisions and then averaging the collision results over the intervening gap [14]. The code itself does not permit to use as an input parameter the charge state, thus the calculations can be considered as a first approximation but according to the experimental results they seem to be accurate enough for nanosecond-scale resolution. The processes of energy loss in the target are: inelastic collision with the atomic electrons of the target, elastic and inelastic collisions with nuclei of target, nuclear reaction, Cerenkov emission. Ionization and recoil in the output tables are referred to the energy loss for ionization (electrons) and recoil (nuclei).

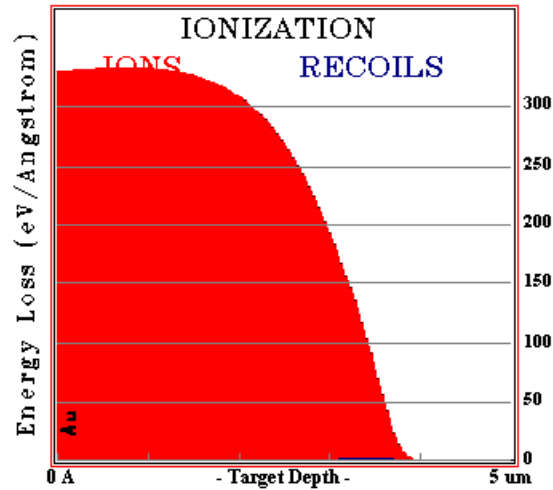


Figure 2.17: Example of the ionization inside the Au target by using TRIM simulation for C with energy of 10 MeV.

As it is shown in the figure 2.17 the energy loss is the red area. The recoils (blue area) are negligible in comparison with the energy loss caused by the ionization. For initial energy peak and energy spread we can use TRIM calculation to obtain the peak of energy and energy spread behind the filter. The two following tables give examples of this technique.

TRIM simulation also showed that for lower initial ion energies there are higher energy losses. As a consequence, it can be seen from table 2.4 and 2.5, the higher is the energy loss (higher energy shift) the higher is the final energy spread at FWHM.

However we calculated that the difference in TOF method for shielded and unshielded IC is negligible due to the distance between the shielding foil and the IC in comparison with the distance between the shielding and the target. If the target-IC distance is 2 m and the shielding-IC distance is 1 mm, ions will fly practically 2 m with the velocity gained during the acceleration and 1 mm slower according to their energy loss. If only high energy ions are in the centre of our interests, the TOF method has a very high accuracy.

Ion Beam	Ion Range ( $\mu\text{m}$ )	Initial Energy $E_i$ (MeV)	Initial FWHM $\sigma_i$ (%)	Final Energy $E_f$ (MeV)	Final FWHM $\sigma_f$ (%)	Energy Shift $\delta E/E_i$ (%)	Peak TOF (ns) at 2 m
H	6.25	1	40	0.77	58.4	23	144
H	195.14	10	40	9.94	40.4	0.6	45.5
H	2860.00	50	40	49.98	40.0	0.04	20
C	2.23	5	40	0.46	169.6	90.8	223
C	20.99	50	40	46.25	45.0	7.5	70
C	236.52	250	40	248.72	40.3	0.5	31
Ti	2.79	18	40	3.88	67.3	78.4	235
Ti	12.86	180	40	147.33	50.2	18.2	74
Ti	78.73	900	40	883.39	41.1	1.8	33.2

Table 2.4: Interaction parameters calculated by using TRIM simulation for a given ion beam in 2  $\mu\text{m}$  Ta filter.

Ion Beam	Ion Range ( $\mu\text{m}$ )	Initial Energy $E_i$ (MeV)	Initial FWHM $\sigma_i$ (%)	Final Energy $E_f$ (MeV)	Final FWHM $\sigma_f$ (%)	Energy Shift $\delta E/E_i$ (%)	Peak TOF (ns) at 2 m
H	14.38	1	40	0.9	47	10	144
H	622.71	10	40	9.98	40.1	0.2	45.5
H	10,750	50	40	49.99	40	0.01	20
C	4.49	5	40	2.39	82.1	52.2	223
C	55.28	50	40	48.72	41.8	2.6	70
C	769.38	250	40	249.64	40.1	0.1	31
Ti	5.76	18	40	9.31	61.1	48.3	235
Ti	32.36	180	40	168.64	43.5	6.3	74
Ti	246.74	900	40	895.2	40.4	0.5	33.2

Table 2.5: Interaction parameters calculated by using TRIM simulation for a given ion beam in 2  $\mu\text{m}$  Al filter.

The increasing transmission of the filter for higher photon energies may be a problem during the measurements as the collector plate works also as a photocathode. The impinging radiation coming from plasma hits the copper plate ejecting electrons from a photocathode. The number of electrons ejected by a single photon with given energy is called quantum efficiency and for Cu photocathode it was measured in [15]. From the figure 2.18 can be seen that a filter transmission more than 10% starts at approximately 600 eV of the photon energy whereas at the same energy the photocathode's quantum efficiency starts to be lower than 0.04 electrons/photon and decreases for higher energies. For this reason the filtering technique eliminates a contribution of the plasma radiation at the output signal.

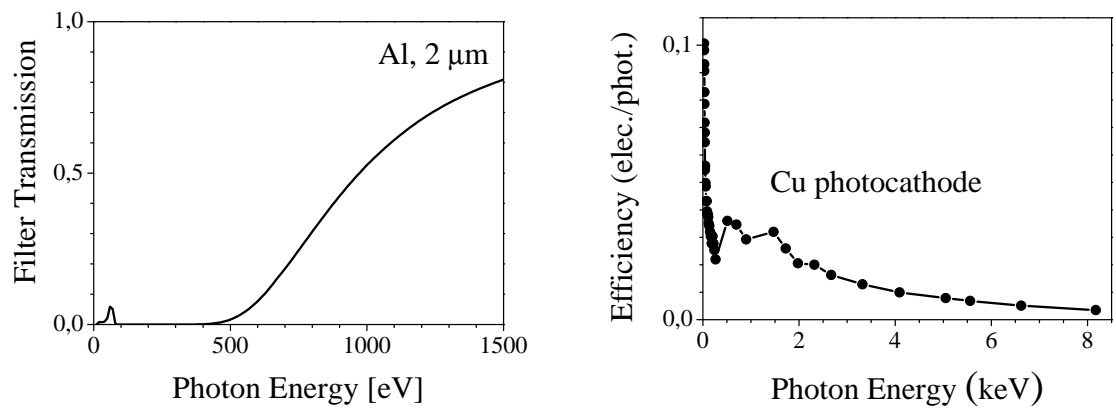


Figure 2.18: Filter transmission of the 2  $\mu\text{m}$  Al filter on the left and quantum efficiency of the Cu photocathode on the right.

## Chapter 3

# Experimental results

The diagnostics system mentioned in previous chapter were tested during the experiment at kJ iodine laser system PALS. The wavelength of the laser beam is 1315 nm and the pulse length is about 300 ps. Laser pulse emitted by the PALS system irradiated the target at angle of  $30^\circ$  with respect to the target normal. The scheme of the experimental setup can be seen on the following figure 3.1. The convention used is that focus position  $FP = 0$  when the minimum focal spot coincides with the target surface, while  $FP < 0$  means that it is located in front of the target surface, and  $FP > 0$  means that it falls inside the target. The diagnostics were positioned in the far expansion zone, i.e. outside of the recombination zone. Thus we can expect that incoming beam is quasi-neutral plasma.

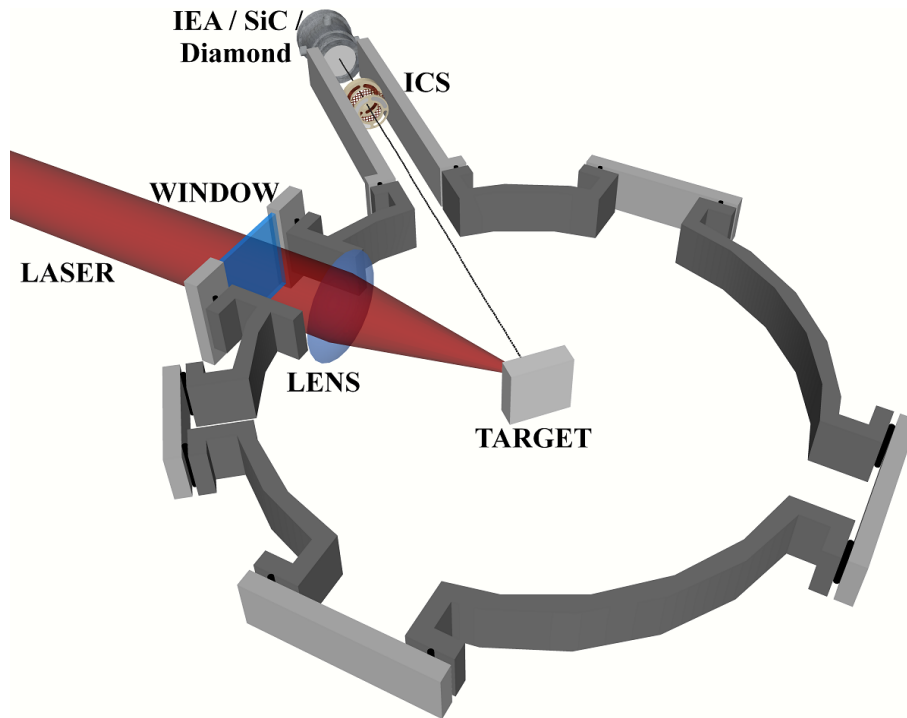


Figure 3.1: The scheme of the spherical chamber at PALS laboratory. The laser beam is coming through the window and is focused by a spherical lens onto the target. The diagnostics are positioned along the target normal direction.

For known  $t_{TOF}$  and target-detector distance  $d$  one can calculate the velocity  $v$  of the ion and its kinetic energy  $E_{KIN}$  as:

$$v = \frac{d}{t_{TOF}} \Rightarrow E_{KIN} = \left( \frac{1}{\sqrt{1 - \frac{v^2}{c^2}}} - 1 \right) m_0 c^2 \quad (3.1)$$

where  $m_0$  is the particle rest mass and  $c$  is speed of light. For the non-relativistic case is valid also:

$$E_{KIN} = \frac{1}{2} m_0 v^2 = \frac{1}{2} m_0 \frac{d^2}{t_{TOF}^2} \quad (3.2)$$

The main tested diagnostics were IC and IEA, Diamond detector and prototype of 4H-SiC nuclear detector. In figure 3.2 we can see the comparison between the IC and the diamond detector. Output signal from the diamond detector give us information that the detector is very sensitive to fast proton signal compared to the IC signal. From formula (2.6) we know that the output current from the diamond detector is proportional to the second power of the velocity and does not depend on the charge state of impinging particles whereas the current from IC given by formula (2.7) is proportional to the velocity linearly and it is proportional to the charge state. Properties similar to the diamond detector also have SiC detector which results can be seen on figure 3.3. Diamond or SiC detectors have to get a certain amount of energy from particles to overcome the energy gap or to create the e-h pair, respectively, therefore they are not sensitive to slow ions which were also confirmed during the measurement (figure 3.2 and 3.3).

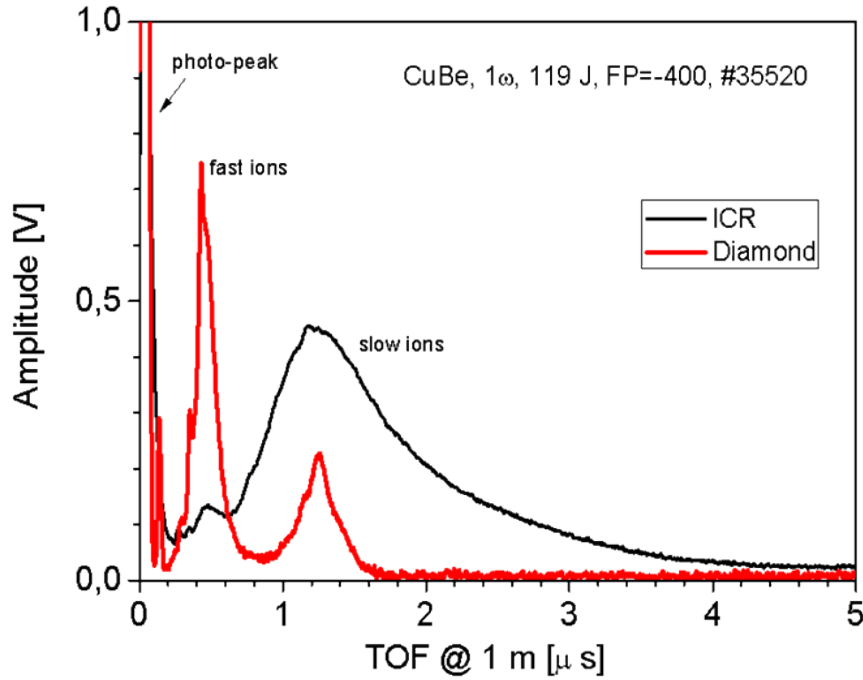


Figure 3.2: The comparison of results from diamond detector and ring IC using a Cu-Be target. The data from measurement are recalculated for both devices as if they would be placed in the same distance from the target.

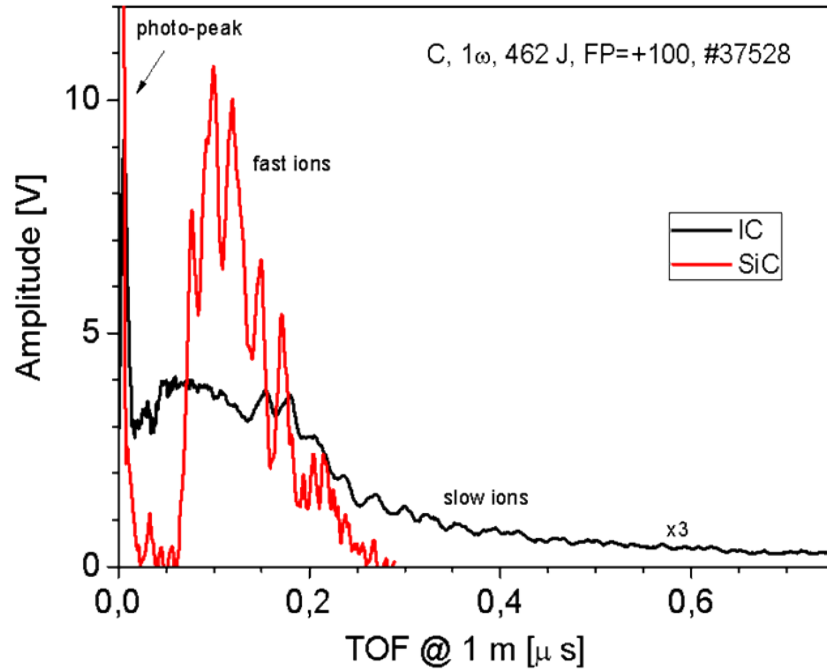


Figure 3.3: The comparison of results from SiC nuclear detector and standard ion collector using graphite target. The data from measurement are recalculated for both devices as if they would be placed in the same distance from the target.

The IC detectors used during the experiment were the flat IC divided into two parts as on figure 2.5 a), the ring IC divided into four parts as on figure 2.6 a) and the solid ring IC as on scheme 2.4. The IC detectors were tested by carbon and hydrogen particle streams coming from graphite target. One of the best results is reported in figure 3.4 where we can clearly see the proof of principle of shielding technique. The photopeak is almost completely stopped by 2  $\mu\text{m}$  thick Al filter and structure of peaks of hydrogen and different ion charge states of carbon is observed. From unshielded ring IC one can see the structure composed of photopeak, fast and slow ions. Slow ions are completely stopped at the filter of shielded IC and this result is in agreement with SRIM calculations.

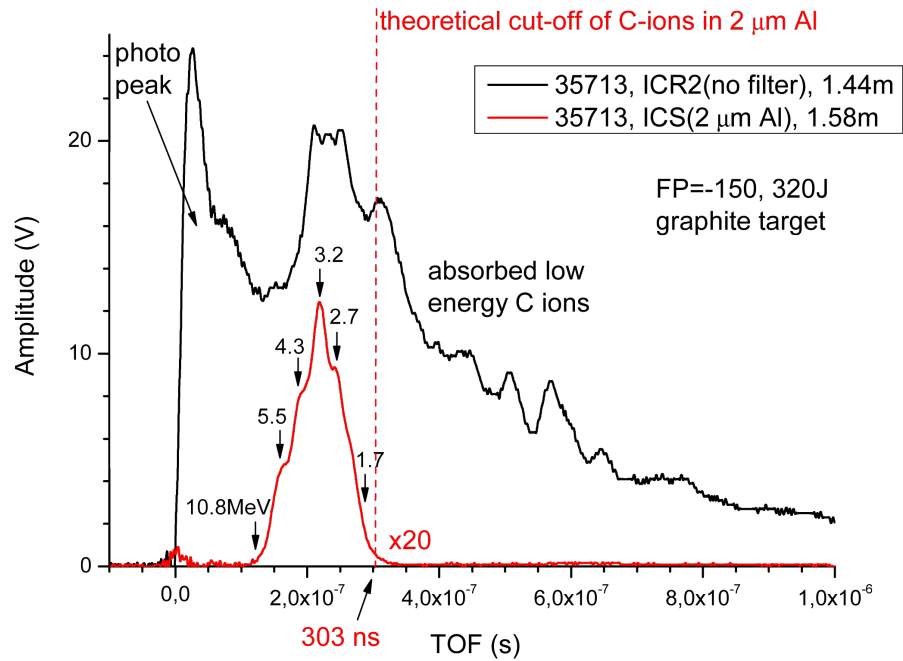


Figure 3.4: Result in TOF measuring using ICS and ICR detectors. The output signal from the ICS is 20 times greater in this figure just to see the clear profile of the shielded collector. It is seen that 2  $\mu\text{m}$  Al foil cut the photopeak and fast ions passed through. The numbers at the partial peaks of the shielded output signal is the energy in MeV of the ions.

Also results from IC shielded collectors showing differences when applying different energies of the laser pulse (as in figure 3.5) on the graphite target. The fastest ions and the highest current are clearly visible in the most energetic laser shot (500 J delivered on target). In 400 J of laser shot one can see approximately the same velocity of the fastest ions as in 312 J laser shot. One can also see that in 400 J shot is smaller current of fast ions than in 312 J shot. One of the possible solutions of this result comes from the theory of acceleration, the highest  $z/A$  ratio has hydrogen ion and any other ion has ratio lower than or equal to this value. Therefore hydrogen is accelerated in lower energetic shots more than other ions because laser does not have enough energy to create high  $z$  heavier ions. The tail of slower ions is coming from heavier particles, they have enough energy to come through filter with a significant loss of energy unlike protons which are stopped completely inside the filter.

Integrating the total charge in figure 3.5 and using TRIM simulations for carbon and hydrogen ions coming through 2  $\mu\text{m}$  Al filter we can estimate amount of detected hydrogen ions in whole beam. The amount of protons in the beam is about 20% of the beam which means  $5 \times 10^{13}$  protons/sr.

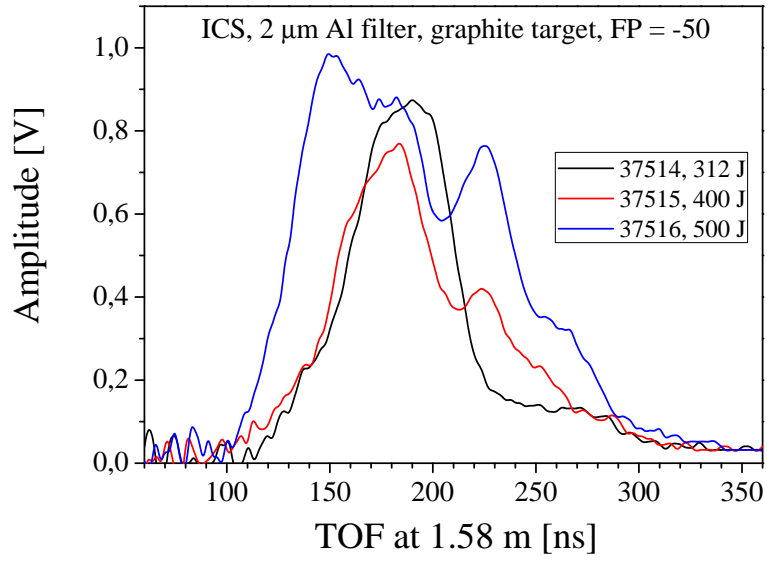


Figure 3.5: Results in TOF measuring using ICS detector with 2  $\mu\text{m}$  Al filter for different laser energies. Focal position for all measurement was set at  $-50 \mu\text{m}$  from graphite target.

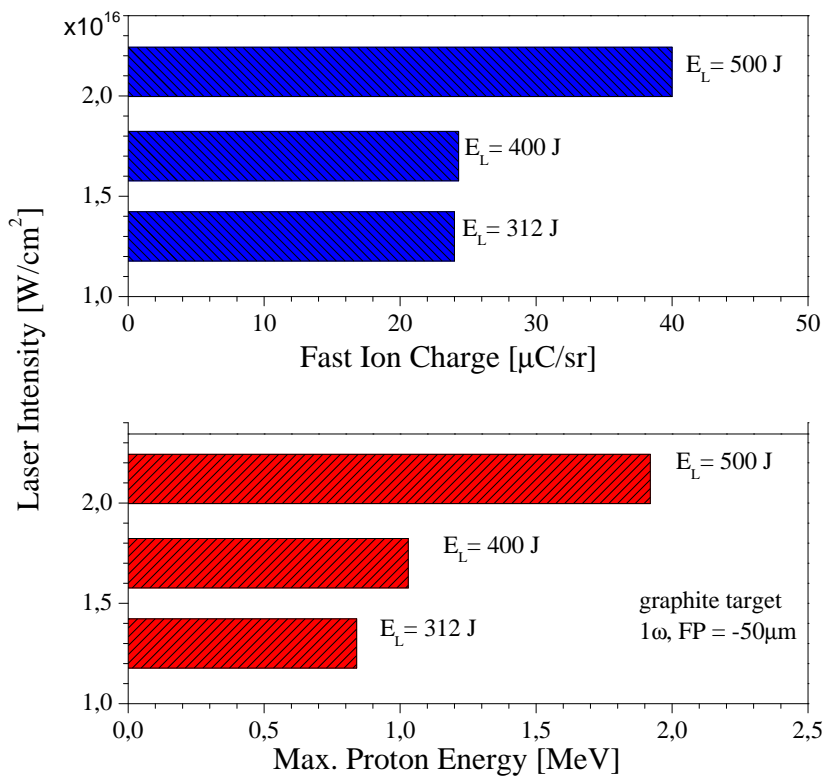


Figure 3.6: Estimation of an ion beam characteristics as an ion charge and maximal energy proton energy.

The aim of our interest was also a new special developed target: hydrogen-enriched silicon; developed at Fondazione Bruno Kessler - IRST in Trento, Italy. This target should provide much more accelerated protons than a pure silicon target with hydrogen impurities absorbed in the atmosphere. Experimental results (as can be seen in figure 3.7 and 3.8) from IEA shows clearly that hydrogen-enriched target produces much higher amount of fast hydrogen ions in comparison with pure silicon target. Comparing the signals also from IC diagnostics in figure 3.9 we can clearly see the increase of more than 200% of proton current in case of using hydrogenized silicon target.

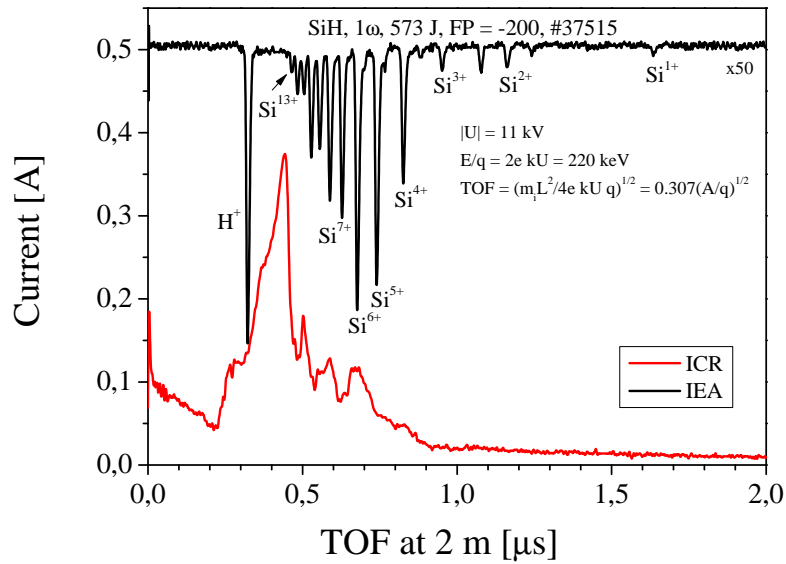


Figure 3.7: TOF spectra obtained from silicon target with hydrogen impurities.

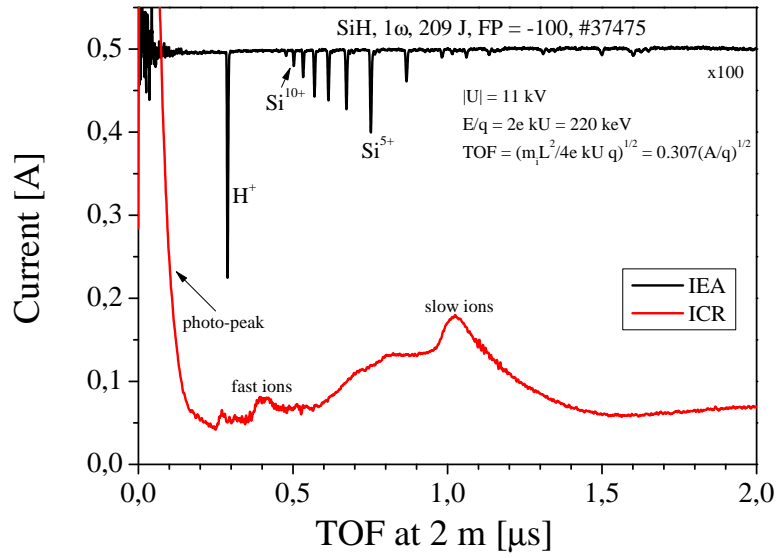


Figure 3.8: TOF spectra obtained from hydrogen-enriched silicon target.

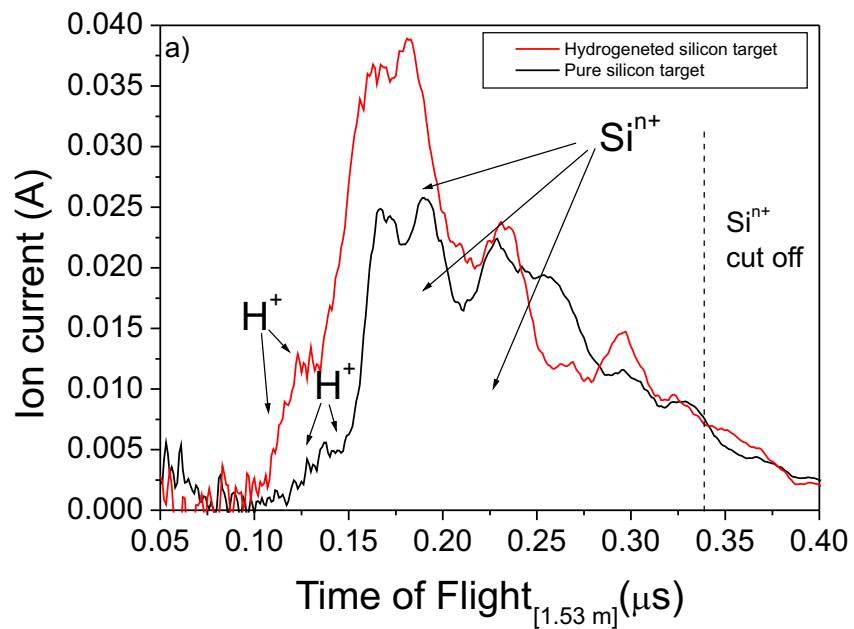


Figure 3.9: Results of TOF filtered IC diagnostics from pure silicon target and hydrogen-enriched silicon target confirming the increase of proton current using enriched target.

# Summary and Conclusions

The diagnostics system described in chapter 2 have been tested in TOF configurations. Diamond detector and a prototype of  $4\text{H-SiC}$  nuclear detectors were successfully tested and results (figure 3.2 and 3.3) confirmed their high sensitivity to fast proton signal and practically no measurable signal to slow ions when comparing to the IC signal coming from the same measurement.

Ion collectors were tested in a shielded and unshielded configurations and the proof of principle of the shielding technique has been performed in experiments (results in figure 3.4 and 3.5). Filter in front of collector does not allow the electromagnetic radiation to come through. Particles with sufficient kinetic energy are not stopped in the filter and they are registered at the output of the detector. The experimental results are in agreement with the SRIM and TRIM simulations described in chapter 2.4.

Newly designed hydrogen-enriched silicon targets were successfully tested with our diagnostics and according to the results (see figure 3.7, 3.8 and 3.9) the amount of hydrogen was increased of more than 200% in comparison with the usage of the pure silicon targets with hydrogen absorbed from the atmosphere.

The future steps will be testing the diagnostics mentioned here in a newly operating Ti-sapphire laser placed also at PALS laboratory. The laser should be able to deliver energy up to 1 J in a 40 fs pulse length. The aim of our interest will be also developing ion collectors in order to place these detectors closer to the target and to get information about the special resolution of plasma particle streams coming from the target.

# Bibliography

- [1] Badziak, J. Laser-driven generation of fast particles. *Opto-Electron. Rev.* **15**, no. 1, 1–12 (2007)
- [2] Hegelich, B. M. *et al.* Laser acceleration of quasi-monoenergetic MeV ion beams. *Nature* **439**, 441–444 (2006)
- [3] Schwoerer, H. *et al.* Laser-plasma acceleration of quasi-monoenergetic protons from microstructured targets. *Nature* **439**, 445–448 (2006)
- [4] Woryna, E. *et al.* Laser and Particle Beams: Pulse Power and High Energy Densities. *Cambridge University press*, 295–306 (1996)
- [5] Isberg, J. *et al.* High carrier mobility in single-crystal plasma deposited diamond. *Science*, vol. **297**, pp. 1670–1672 (2002)
- [6] Galbiati, A. *et al.* Performance of Monocrystalline Diamond Radiation Detectors Fabricated Using TiW, Cr/Au and a Novel Ohmic DLC/Pt/Au Electrical Contact. *IEEE Transactions on Nuclear Science*, vol. **56**, no. 4, pp. 1863–1874 (August 2009)
- [7] Gudden, B. and Pohl, R. Über lichtelektrische Leitfähigkeit von Diamanten. *Zeitschrift für Physik A Hadrons and Nuclei*, vol. **3**, no. 2, pp. 123–129 (March 1920)
- [8] van Herdeen, P. J. The crystal counter, a new instrument in nuclear physics. *Ph.D. dissertation*, University of Utrecht, Utrecht, The Netherlands, 1945
- [9] Hofstadter, R. Remarks on diamond crystal counters. *Phys. Rev.*, vol. **73**, p. 631 (1948)
- [10] Torrisi, L. *et al.* Single Crystal Silicon Carbide Detector of Emitted Ions and Soft X-rays from Power Laser-generated Plasmas. *Journal of Applied Physics*, vol. **105**, 123304 (2009)
- [11] Moscatelli, F. *et al.* Annealing Effects on Leakage Current and Epilayer Doping Concentration of p+n Junction 4H-SiC Diodes after Very High Neutron Irradiation. *Nuclear Instruments and Methods in Physics Research Section A: Accelerators, Spectrometers, Detectors and Associated Equipment*, vol. **583**, pp. 173–176 (2007)
- [12] Puglisi, D. SiC Nuclear Detector. *Ph.D. dissertation*, Catania University, Italy, 2009
- [13] [http://henke.lbl.gov/optical\\_constants/filter2.html](http://henke.lbl.gov/optical_constants/filter2.html)  
(Accessed June 15, 2009)
- [14] <http://www.srim.org/>  
(Accessed June 15, 2009)

- [15] Day, R. H. *et al.* Photoelectric quantum efficiencies and filter window absorption coefficients from 20 eV to 10 keV. *J. Appl. Phys.*, vol. **52**, no. 11, pp. 6965–6973 (November 1981)
- [16] Margarone, D. *et al.* Diamond detectors for characterization of laser-generated plasma. *Radiation Effects Defects in Solids*, vol. **163**, nos. 4–6, pp. 463–470 (April–June 2008)